J Solid State Electrochem (2011) 15:277–284
DOI 10.1007/s10008-010-1208-4

ORIGINAL PAPER

Electrical conductivity and defect chemistry of $Ba_xSr_{1-x}Co_yFe_{1-y}O_{3-\delta}$ perovskites

Zhèn Yáng · Ashley S. Harvey · Anna Infortuna · Joop Schoonman · Ludwig J. Gauckler

Received: 26 April 2010 / Revised: 21 September 2010 / Accepted: 23 September 2010 / Published online: 15 October 2010

Abstract Bulk $Ba_xSr_{1-x}Co_yFe_{1-y}O_{3-\delta}$ compositions (BSCF) were synthesized by the solid-state reaction method. The electrical conductivity of ceramic bars was measured using a dc four-probe method as a function of temperature in air up to 970 °C. All compositions showed thermally activated *p*-type semi-conductivity up to ~450 °C and then a transition to metal-like conductivity. The small-polaron hopping *p*-type semi-conductivity depends on the oxygen nonstoichiometry, which increases with increasing temperature. Metal-like conductivity is attributed to the overlap of the transition metal *d*-electron orbitals with the oxygen *p*-orbitals. Strontium-rich compositions show higher conductivity. The Co/Fe ratio does not influence much the *p*-type semi-conduction. Iron-rich compositions revealed more metal-like conduction behavior. The degree of overlap between transition metal *d*-orbitals and oxygen *p*-orbitals depends on the Ba/Sr as well as on the Co/Fe ratios.

Keywords Electrical conductivity · BSCF · Mixed ionic and electronic conduction · Perovskite · Metal-insulator transition · Cathode · Solid oxide fuel cell · Catalysis

Z. Yáng (✉) · A. S. Harvey · A. Infortuna · L. J. Gauckler
Nonmetallic Inorganic Materials, Department of Materials,
ETH Zurich,
8093 Zurich, Switzerland
e-mail: zhen.yang@mat.ethz.ch

J. Schoonman
Section Materials for Energy Conversion and Storage, Department Chemical Engineering, Delft University of Technology,
Julianalaan 136,
2628 BL Delft, The Netherlands

Introduction

The solid oxide fuel cell (SOFC) is an electrochemical device that converts chemical energy directly into electricity using hydrocarbon fuel and oxygen at high temperatures [1]. Perovskite-type materials exhibit good oxygen catalytic activity and high mixed ionic-electronic conductivity. Materials like lanthanum manganite [2], lanthanum cobaltite [3], strontium-doped lanthanum manganite [4], strontium- and cobalt-doped lanthanum ferrite [5, 6], and strontium-doped samarium cobaltite [7] have been widely studied as SOFC cathodes as well as for catalysis [8]. In addition, $Ba_{0.5}Sr_{0.5}Co_{0.8}Fe_{0.2}O_{3-\delta}$ was reported first in 2000 as an oxygen permeation membrane material [9] by Shao et al., who also reported $Ba_{0.3}Sr_{0.7}Co_{0.8}Fe_{0.2}O_{3-\delta}$ to exhibit the highest oxygen permeability in the $Ba_xSr_{1-x}Co_{0.8}Fe_{0.2}O_{3-\delta}$ family [10]. This composition was reported as a possible novel high-performance cathode material with low polarization resistance in the intermediate temperature range 500–700 °C [11].

Different researchers have reported in recent years the electrical conductivity of $Ba_{0.5}Sr_{0.5}Co_{0.8}Fe_{0.2}O_{3-\delta}$, i.e., Jiang et al. observed a maximum of conductivity to occur around 470 °C both on heating and cooling, which was related to the oxygen nonstoichiometry changes with temperature [12]. Li et al. found the electrical conductivity to reach over 300 S/cm in the temperature range 500–800 °C [13]. Wei et al. reported the electrical conductivity as a function of temperature in both air and nitrogen atmospheres and observed that the material behaves differently above 450 °C depending on the ambient gas atmosphere. In air the electrical conductivity starts to decrease slowly upon further heating, while in nitrogen it keeps on increasing up to 900 °C [14]. Ge et al. investigated the electrical conductivity of A-site and B-site

deficient $(Ba_{0.5}Sr_{0.5})_{1-x}(Co_{0.8}Fe_{0.2})_{1-y}O_{3-\delta}$. They found the electrical conductivity to decrease with increasing cation deficiency on both sites for x=0–0.15 [15] and y=0–0.17 [16], respectively. Several publications report on the electrical conductivity of the entire $Ba_xSr_{1-x}Co_yFe_{1-y}O_{3-\delta}$ (BSCF) system in order to obtain a better understanding of relations between the electrical properties and the stoichiometries. Zeng et al. reported that barium-free $SrCo_{0.8}Fe_{0.2}O_{3-\delta}$ exhibits a higher electrical conductivity than $Ba_{0.5}Sr_{0.5}Co_{0.8}Fe_{0.2}O_{3-\delta}$ [17], and Wei et al. observed the electrical conductivity of $Ba_xSr_{1-x}Co_{0.8}Fe_{0.2}O_{3-\delta}$ (x= 0.3–0.7) to decrease with increased Ba doping [18]. Chen et al. studied the influence of the Co/Fe ratio on the electrical conductivity of $Ba_{0.5}Sr_{0.5}Co_{1-y}Fe_yO_{3-\delta}$ (y=0.0–1.0) in oxygen, air, and argon atmospheres. Their data revealed an increased p-type conductivity with increasing Co content [19]. Zhao et al. studied the electrical conductivity of eight compositions of the $Ba_xSr_{1-x}Co_yFe_{1-y}O_{3-\delta}$ system in the temperature range 300–800 °C in air [20] and observed that BSCF samples with increasing Ba or Co contents exhibit a decreasing electrical conductivity.

Although the electrical conductivity of several compositions in the BSCF system was investigated in detail, a thorough understanding of the conduction mechanism and defect chemistry has not yet been reported for different Ba to Sr and Co to Fe ratios. In this work $Ba_xSr_{1-x}Co_yFe_{1-y}O_{3-\delta}$ compositions with x=0.2, 0.4, 0.5, and 0.6 and y=0.2, 0.4, 0.6, and 0.8 were synthesized, and the electrical conductivity of bulk polycrystalline samples and relative oxygen stoichiometry changes were investigated in air from room temperature to 970 °C in order to understand the conduction mechanism of the non-stoichiometric perovskites $Ba_xSr_{1-x}Co_yFe_{1-y}O_{3-\delta}$.

Experimental

The BSCF powders were synthesized by the solid-state reaction method as described in detail in a previous publication [21] in which the phase relations were reported as well. The finely ground green powders were calcined for 6 h at 1,000 °C in air. The calcined powders were planetary milled and ground. The crystalline phase of the calcined powder was identified by means of X-ray diffraction (XRD). Powder samples were scanned from 10° to 90° with a step size of 0.02° at a scanning speed of 15 s/step for 2θ in a Siemens Bruker X-ray Diffractometer with a $Cu-K_\alpha$ monochromator. Thermogravimetric measurements were performed using a NETZSCH STA 449 C thermobalance by cycling twice the samples in the temperature range 100–1,000 °C at a rate of 1 °C/min in synthetic air atmosphere. The resulting mass change was calibrated by taking an empty alumina crucible as a reference in the same temperature range and the same synthetic air atmosphere. Calcined powders were uniaxially pressed to shape bulk specimen bars of 55×5×2.5 mm^3. These green bars were cold iso-statically pressed for 3 min at a pressure of 283 MPa. They were sintered at 1,100 °C for 6 h in air. For density measurements, the sintered bulk specimens were weighed in deionized water (0.9968 g/cm^3, 26 °C) for determining their Archimedes density. For each composition, more than three samples were measured and the mean value including one standard deviation as error is given in Table 1. A dc four-probe method was used to measure the resistance of the specimen bars. Platinum wires were used as electrodes and were glued onto the sample with a platinum-containing conductive paste for a better contact. The samples were heated in a tubular furnace with ramp rates of 0.1, 1, and 10 °C/min from room temperature up to 970 °C with twice thermal cycling in air. Sintered bulk specimens were polished with a fine diamond polishing pad on cross-sections for microstructural characterization with scanning electron microscopy (Leo 1530). A Seebeck effect qualitative test was performed on a sintered Φ=25 mm, 5-mm thick pellet, with two probes on both sides of the pellet. The voltage bias was measured between the hot probe (25–400 °C) and the room-temperature probe in air.

Results

Powder crystalline phase and bulk density

Calcined powders at 1,000 °C of $Ba_xSr_{1-x}Co_yFe_{1-y}O_{3-\delta}$ (x=0.2, 0.4, 0.5, and 0.6 and y=0.2, 0.4, 0.6, and 0.8) represent pure cubic perovskites. Their lattice parameters were reported in previous work [21]. The lattice parameters increase with increasing barium content and slightly increase with replacing iron by cobalt. This is reasonable for the A-site doping, because the larger barium cations ($r_{Ba^{2+}} = 1.61$ A, $r_{Sr^{2+}} = 1.44$ A, for coordination number 12 [22]) increase the unit cell. While doping with cobalt on the B-site caused a slight expansion of the unit cell, this is in contrast to the ratio of the ionic radii of iron and cobalt ions, because the iron cation is always larger than the cobalt cation for the same condition including the coordination, the valence state, and the spin state [22]. We also have synthesized the composition x=0.8 with y=0.8. However, this sample showed a hexagonal phase besides a cubic phase [21]. We will report about this material's properties separately as the material undergoes a reversible phase change upon thermal cycling between room temperature and 1,000 °C.

The sintered bulk ceramics have closed pores with sizes of a few microns, i.e., from 1 to 10 μm (Fig. 1). The Archimedes densities ρ_{bulk} of sintered bulk specimens are

Table 1 The Archimedes density ρ_{bulk} (g/cm^3), the theoretical density ρ_{theo} (g/cm^3), and the volume density ρ_v (%) of BSCF compositions

	$Ba_xSr_{1-x}Co_{0.8}Fe_{0.2}O_{3-\delta}$				$Ba_{0.5}Sr_{0.5}Co_yFe_{1-y}O_{3-\delta}$		
	ρ_{bulk}	ρ_{theo}	ρ_v		ρ_{bulk}	ρ_{theo}	ρ_v
x=0.2	4.9204±0.0327	5.7550	88.35±0.78%	y=0.2	5.1867±0.0335	5.8533	89.26±1.28%
x=0.4	4.9393±0.0207	5.7342	86.99±2.93%	y=0.4	5.0700±0.1565	5.8477	90.26±1.51%
x=0.6	4.9030±0.1205	5.8391	81.86±3.64%	y=0.6	4.9572±0.0100	5.8244	89.98±0.88%
				y=0.8	4.9348±0.0930	5.8013	90.79±0.96%

listed in Table 1. The volume density of sintered samples was estimated by considering the porosity, which was determined on cross-sections of the specimens by optical microscopy using the linear intercept method for the pores by a software Lince from TU Darmstadt, Germany (see Table 1).

Kinetics of electrical conductivity by thermal cycling

The electrical conductivity was measured at different heating rates in order to evaluate the conditions for equilibrium values. The electrical conductivity of a sintered specimen bar $Ba_{0.5}Sr_{0.5}Co_{0.8}Fe_{0.2}O_{3-\delta}$ ($17.1 \times 4.6 \times 2.3$ mm^3) was, therefore, measured using three different ramp rates, i.e., 10 (Fig. 2a), 1, and 0.1 °C/min (Fig. 2b). At a rate of 10 °C/min large hysteresis of the electrical conductivity as a function of temperature was observed, especially above 450 °C, whereas the slower rate of 0.1 °C/min resulted in much smaller hysteresis. This indicates that the BSCF materials attain an equilibrium state very slowly. Therefore, the electrical conductivity measurements as a function of temperature were performed at a relatively low temperature rate, i.e., 1 °C/min, in order to approach equilibrium for the oxygen stoichiometry and the electrical conductivity. In the following, the electrical conductivity data are the cooling curve data of the second cycle in the temperature range 85–970 °C for all compositions in order to have a consistent comparison at a cooling rate of 1 °C/min for the equilibrium electrical conductivity.

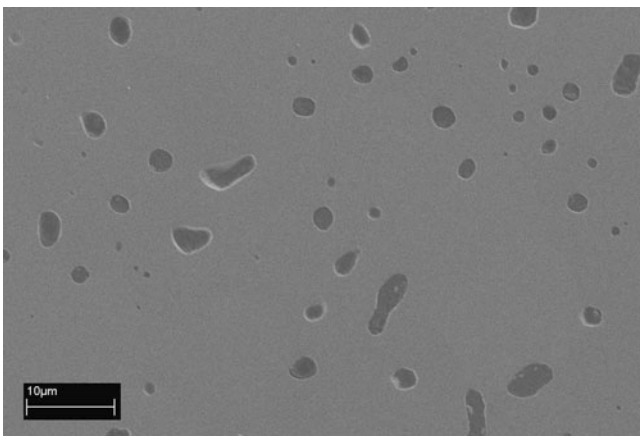

Fig. 1 Microstructure of a polished cross-section of one representative composition $Ba_{0.5}Sr_{0.5}Co_{0.6}Fe_{0.4}O_{3-\delta}$, sintering treatment is heating at 1,100 °C for 6 h in air

Electrical conductivity

The temperature-dependence of the electrical conductivity of $Ba_xSr_{1-x}Co_{0.8}Fe_{0.2}O_{3-\delta}$ and of $Ba_{0.5}Sr_{0.5}Co_yFe_{1-y}O_{3-\delta}$

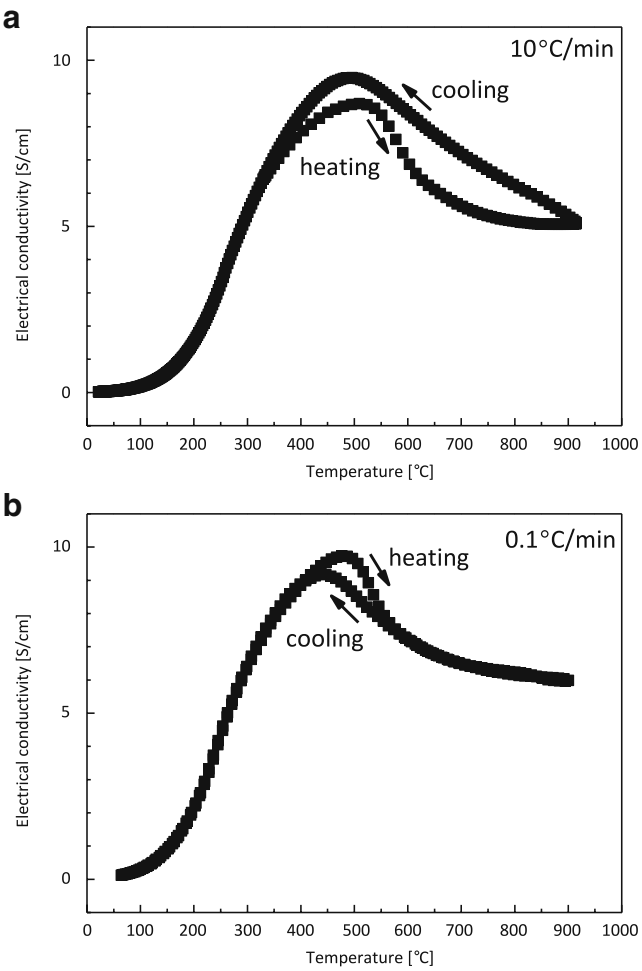

Fig. 2 The electrical conductivity of a $Ba_{0.5}Sr_{0.5}Co_{0.8}Fe_{0.2}O_{3-\delta}$ sintered bulk specimen bar in ambient air during heating and cooling cycles with a rate of **a** 10 °C/min and **b** 0.1 °C/min

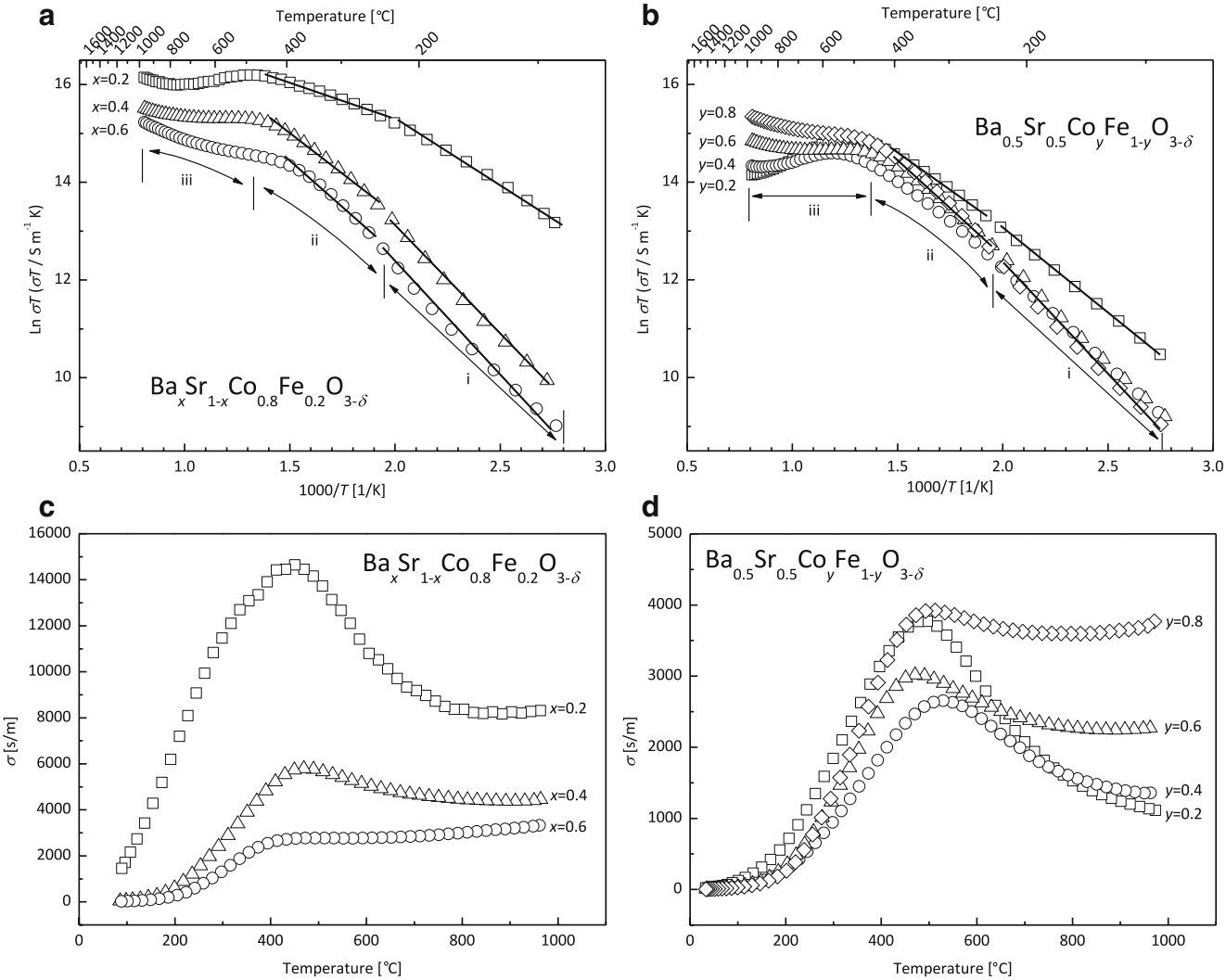

Fig. 3 The Arrhenius plots of the electrical conductivity of **a** $Ba_xSr_{1-x}Co_{0.8}Fe_{0.2}O_{3-\delta}$ ($x=0.2$, 0.4, and 0.6) and **b** $Ba_{0.5}Sr_{0.5}Co_yFe_{1-y}O_{3-\delta}$ (y=0.2, 0.4, 0.6, and 0.8) in air. *Lines* are visual guides for the eyes. The electrical conductivity of **c** $Ba_xSr_{1-x}Co_{0.8}Fe_{0.2}O_{3-\delta}$ ($x=0.2$, 0.4, and 0.6) and **d** $Ba_{0.5}Sr_{0.5}Co_yFe_{1-y}O_{3-\delta}$ (y=0.2, 0.4, 0.6, and 0.8) as a function of temperature in air

is presented in Fig. 3a–d, respectively. From room temperature up to 450 °C *p*-type semi-conductivity [19] is observed. This *p*-type conductivity was proved by the qualitative Seebeck test revealing the charge carriers to be holes. For higher temperatures there exists a deviation from semi-conductivity (x=0.6 and y=0.8) and in most samples, even a metal-like conductivity from 450 to 900 °C. $Ba_{0.2}Sr_{0.8}Co_{0.8}Fe_{0.2}O_{3-\delta}$ exhibits with $\sigma=1.46\times10^4$ S/m at 450 °C a maximum electrical conductivity of all $Ba_xSr_{1-x}Co_{0.8}Fe_{0.2}O_{3-\delta}$ (x=0.2, 0.4, 0.5, and 0.6) compositions. Strontium-rich compositions have higher electrical conductivity than barium-rich compositions in the whole temperature range from room temperature to 970 °C. This is in agreement with the literature [18, 20]. The strontium-rich compositions also have a stronger metal-like conduction behavior above the transition temperature than the barium-rich compositions. $Ba_{0.5}Sr_{0.5}Co_{0.8}Fe_{0.2}O_{3-\delta}$ exhibits with $\sigma=3.9\times10^3$ S/m at 505 °C the maximum electrical conductivity of all $Ba_{0.5}Sr_{0.5}Co_yFe_{1-y}O_{3-\delta}$ (y=0.2, 0.4, 0.6, 0.8) compositions. Iron-rich compositions have higher electrical conductivity below the transition temperature and a stronger metal-like conduction behavior above the transition temperature than the cobalt-rich compositions.

The electrical conductivity is shown in Arrhenius plots in Fig. 3a, b. There are two kinds of charge carriers in these materials, holes and oxygen vacancies [23]. Because the mobility of oxygen ions is much lower than that of the electron holes, it can be assumed that the measured electrical

conductivities represent only the electronic conductivity. The temperature-dependent electrical conductivity of the transition metal containing perovskites can be described by a small-polaron hopping mechanism expressed by Eq. 1:

$$\sigma = \left(\frac{A}{T}\right) \exp\left(-\frac{E_a}{kT}\right) \quad (1)$$

where E_a is the activation energy, k is the Boltzmann constant, T is the absolute temperature, A is a characteristic parameter for the specific material, and σ is the electrical conductivity in the unit of S/m [24–29]. We can distinguish a rather linear part of the $\ln\sigma T$ versus $1/T$ curves from room temperature to 240 °C and a deviation from the linear behavior above 240 °C. For temperatures up to 240 °C the activation energies, denoted as E_{a1}, are listed in Table 2. We find activation energies from 0.22 to 0.42 eV (corresponding to 21–41 kJ/mol) which is in good agreement with earlier findings by Wei et al. [18]. Sr-rich compositions have lower activation energies than Ba-rich ones, and Fe-rich compositions have lower activation energies than Co-rich ones. In this temperature regime up to 240 °C we do not observe any weight loss due to oxygen desorption as shown in Fig. 4. Above 240 °C we find that the activation energies denoted as E_{a2} being smaller than those in the region (i). In this temperature regime, we observe weight loss starting at 240 °C due to oxygen desorption as shown in Fig. 4, the oxygen loss causes a decrease in the number of electronic charge carriers as will be discussed later.

From 450 to 900 °C, we observe a deviation from semi-conducting behavior. The transition temperature from semi-conductivity to metal-like conductivity of $Ba_xSr_{1-x}Co_{0.8}Fe_{0.2}O_{3-\delta}$ is between 410 and 490 °C. It is slightly lower for Sr-rich compositions. For the Ba/Sr=1 samples, the transition temperature is between 450 and 550 °C. The observed transitions from semi-conductivity to metal-like conductivity are not due to a phase transition, as the phase stability was investigated by previous in situ high-temperature XRD characterizations of the same material, i.e., $Ba_{0.5}Sr_{0.5}Co_{0.8}Fe_{0.2}O_{3-\delta}$, and the cubic phase was found in the temperature regime from room temperature to 1,000 °C in air [21, 30, 31].

Upon heating the specimens loose oxygen even in air. The oxygen content $3-\delta$ of the $Ba_{0.5}Sr_{0.5}Co_yFe_{1-y}O_{3-\delta}$ materials as a function of temperature was measured by recording the mass change of the powder samples by the thermogravimetric method and the results are shown in Fig. 4. The starting reference value of $3-\delta$ was normalized as 3.0 in order to have a relative comparison of the change of the oxygen content as a function of temperature. BSCF materials exhibit reversible oxygen loss and pick-up characteristics during heating and cooling cycles at a rate of 1 °C/min. In Fig. 4, the oxygen loss starts at 240 °C in accordance with reported data [14]. In the high-temperature range 600–1,000 °C, the oxygen loss is smaller than at temperatures below 600 °C. The change of oxygen content in $Ba_{0.5}Sr_{0.5}Co_yFe_{1-y}O_{3-\delta}$ (y=0.2–0.8) in different temperature regions is shown as a function of the cobalt content (Fig. 5). It decreases with increasing Co content, except for $Ba_{0.5}Sr_{0.5}Co_{0.8}Fe_{0.2}O_{3-\delta}$, as the oxygen nonstoichiometry in this composition is slightly higher than that in the composition x=0.5 with y=0.6. Iron-rich compositions have higher oxygen loss than cobalt-rich compositions. This is correlated with the stronger metal-like conductivity at high temperatures as will be discussed later.

Defect chemistry

In the ideal ABO_3 perovskite materials, we assume that the Ba and Sr ions are on the A sites, Fe and Co ions are on the B-sites, and that the transition metal ions are in a tetravalent state: $A^{2+}B^{4+}O_3^{2-}$ based on the charge neutrality rule. In (Ba_xSr_{1-x}) $(Co_yFe_{1-y})O_3$, the A′ and A″ ions have fixed

Table 2 The activation energies E_{a1} (below 240 °C) and E_{a2} (240 °C—transition temperature; unit, eV) calculated from the electrical conductivity data using a small-polaron hopping model

	E_{a1} (eV)	E_{a2} (eV)
$Ba_{0.5}Sr_{0.5}Co_{0.2}Fe_{0.8}O_{3-\delta}$	0.30	0.24
$Ba_{0.5}Sr_{0.5}Co_{0.4}Fe_{0.6}O_{3-\delta}$	0.34	0.28
$Ba_{0.5}Sr_{0.5}Co_{0.6}Fe_{0.4}O_{3-\delta}$	0.38	0.30
$Ba_{0.5}Sr_{0.5}Co_{0.8}Fe_{0.2}O_{3-\delta}$	0.42	0.34
$Ba_{0.2}Sr_{0.8}Co_{0.8}Fe_{0.2}O_{3-\delta}$	0.22	0.12
$Ba_{0.4}Sr_{0.6}Co_{0.8}Fe_{0.2}O_{3-\delta}$	0.41	0.28
$Ba_{0.6}Sr_{0.4}Co_{0.8}Fe_{0.2}O_{3-\delta}$	0.42	0.33

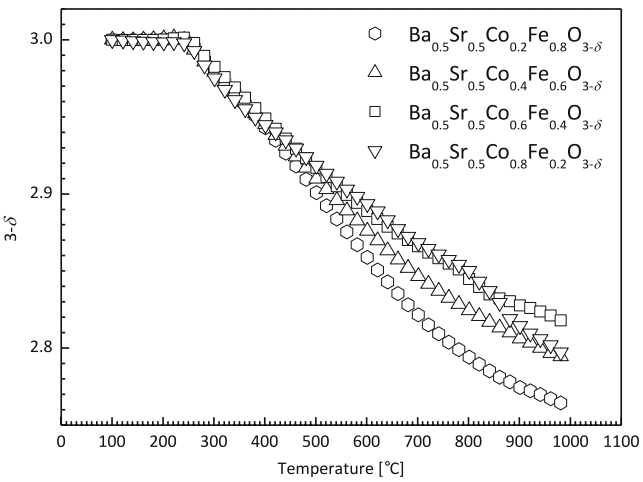

Fig. 4 Oxygen content as a function of temperature for the powder specimens $Ba_{0.5}Sr_{0.5}Co_yFe_{1-y}O_{3-\delta}$ (y=0.2, 0.4, 0.6, and 0.8) in synthetic air atmosphere

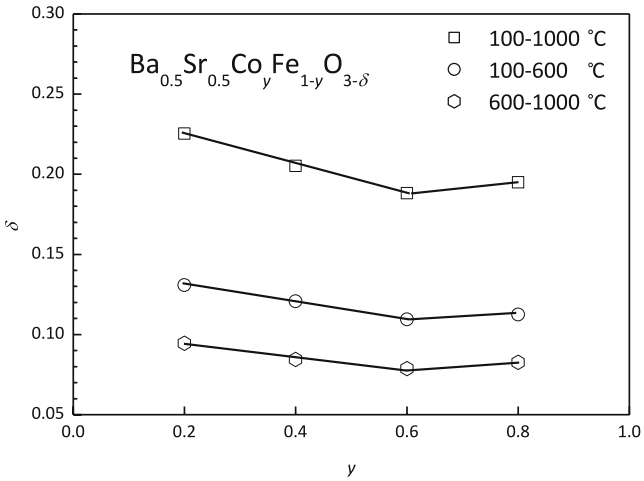

Fig. 5 Oxygen nonstoichiometry as a function of cobalt content in $Ba_{0.5}Sr_{0.5}Co_yFe_{1-y}O_{3-\delta}$ (y=0.2, 0.4, 0.6, and 0.8). *Lines* are visual guides for the eyes

valence states of +2. Now, we use the Kröger–Vink defect notation to illustrate the deviations from stoichiometry. Upon heating, the sample looses oxygen and the oxygen nonstoichiometry is then expressed by:

$$O_O^X + 2h^\bullet \Leftrightarrow \frac{1}{2}O_2(g)\uparrow + V_O^{\bullet\bullet} \tag{2}$$

Oxygen vacancies ($V_O^{\bullet\bullet}$) with an effective charge +2q are introduced into the lattice and holes ($h^\bullet$) are consumed. In addition, the transition metal cations are reduced, as presented by the following lattice reactions:

$$Co_{Co}^X \Leftrightarrow Co_{Co}^{'} + h^\bullet \tag{3}$$

$$Fe_{Fe}^X \Leftrightarrow Fe_{Fe}^{'} + h^\bullet \tag{4}$$

Upon this reduction of the cations, holes ($h^\bullet$) are created. As the measured oxygen loss, when heating the materials (as shown in Fig. 4) has to be attributed to the formation of oxygen vacancies and the simultaneously occurring reduction of Fe and Co, we can write Eqs. 3 and 4 together with Eq. 2 as follows:

$$2\,Co_{Co}^X + O_O^X \Leftrightarrow 2\,Co_{Co}^{'} + V_O^{\bullet\bullet} + \frac{1}{2}O_2(g)\uparrow \tag{5}$$

$$2\,Fe_{Fe}^X + O_O^X \Leftrightarrow 2\,Fe_{Fe}^{'} + V_O^{\bullet\bullet} + \frac{1}{2}O_2(g)\uparrow \tag{6}$$

BSCF compositions at room temperature contain oxygen vacancies ($V_O^{\bullet\bullet}$) and holes ($h^\bullet$) [32]. Upon heating beyond 240 °C, the material looses oxygen and the concentration of oxygen vacancies increases while at the same time the concentration of electron holes, responsible for the p-type semi-conductivity, are consumed by lattice reaction 2. At the same time, the reduction of the transition metal cations occurs (Eqs. 3 and 4) and creates new holes ($h^\bullet$). Their effective charges are compensated by the charges of the oxygen ion vacancies.

At higher temperatures (>900 °C) the following lattice reaction might become important, i.e.,

$$Co_{Co}^{'} \Leftrightarrow Co_{Co}^{''} + h^\bullet \tag{7}$$

The further reduction of Co^{3+} to Co^{2+} produces electron hole carriers. Therefore, at high temperatures, Eqs. 2, 3, 4, and 7 may represent the lattice reactions of oxygen vacancy generation, transition metal cation reduction, and electron hole consumption and generation.

Discussion of electrical conductivity

From room temperature to 240 °C, the BSCF materials exhibit p-type semi-conductivity and have already a high oxygen nonstoichiometry [32], e.g., $Ba_{0.5}Sr_{0.5}Co_{0.8}Fe_{0.2}O_{3-\delta}$, is already oxygen deficient at room temperature with $3-\delta$= 2.39 after [32]. With the fixed valence states of 2+ for Ba and Sr it follows then an average valence state of B-site cations of 2.78+ at room temperature. These multi-valence states [33] of the transition metal cations on the B-sites form the basis of small-polaron hopping between the B–O–B bonds and hence the observed semi-conductivity as further described in [33, 34] by Harvey et al.

From 240 to 450 °C, the oxygen desorption starts and the material becomes more oxygen deficient. Therefore, oxygen vacancies are generated in the lattice according to the lattice reaction 2 and further reduction of the transition metal cations occurs while the consumption of electron holes occurs as well. This leads to the situation, that two charge states exist, one between Fe^{4+} and Fe^{3+} and one between Fe^{3+} and Fe^{2+} [33]. After [33] the highest starting oxidation state of Co is close to Co^{3+}. Co reduces then to a 2+ state at temperatures higher than 900 °C [33] according to the lattice reaction 7. Arnold et al. have studied the temperature-dependent local charge disproportionation in the $(Ba_{0.5}Sr_{0.5})(Co_{0.8}Fe_{0.2})O_{3-\delta}$ material by in situ EELS measurements [35]. They found that the valence of Co changes from 2.6+ at room temperature to 2.2+ at 500 °C and with further heating, they found no valence change any more for Co. Similarly, they found the valence of Fe to change from 3.0+ at room temperature to 2.8+ at 500 °C and no further valence change is observed for Fe at higher temperatures in their study.

From the transition temperature, i.e., 450 °C, up to 970 °C some of BSCF materials show metal-like

conductivity (see Fig. 3c, d), i.e., a decreased conductivity with increasing temperature. This was also observed for the cobalt- and iron-containing systems $Sr_{1-x}Ce_xFe_{1-y}Co_yO_{3-\delta}$ [36] and $La_{1-x}Sr_xCoO_3$ [37]. The small-polaron hopping model is not able to explain this electrical conductivity behavior in this temperature regime. In transition metal containing perovskites, the *d*-electrons experience two competing forces: (1) coulombic repulsion tends to localize the individual *d*-electrons at atomic lattice sites at lower temperatures and (2) hybridization with oxygen *p* electron states tends to delocalize the electrons [38] at higher temperatures. As a consequence of the latter, the t_{2g} orbitals of the transition metal ions and the p_π orbitals of the oxygen ions start to overlap due to the reduced oxidation state of the transition metal cations with increasing temperatures above 450 °C. This generates a state of delocalized charge carriers, as it was pointed out already earlier [39]. These delocalized charge carriers dominate the electrical conductivity of the BSCF materials at high temperatures (>450 °C) resulting in metal-like conductivity. In addition, as we have introduced oxygen vacancies upon heating these vacancies might act as scattering centers for the charge carriers reducing their mobility. This is particularly expressed stronger for the Fe-rich compositions than for the Co-rich ones (see Figs. 3d and 4). This can be rationalized as follows:

In the cubic perovskite ABO_3, there are three collinear –O–B–O–B–O– chains along the principal directions *x*, *y*, and *z*. These chains form the conduction pathways for the electron holes. The most important fact for metal-like conduction is the overlap of the transition metal *d*-orbitals (t_{2g}) and oxygen p_π orbitals, i.e., $-B_{t_{2g}} - O_{p_\pi} - B_{t_{2g}}-$ [39]. The attractive potential between B and O in neighboring B–O pairs is higher than that of A and O in the A–O pairs. An increasing attractive lattice potential $U \propto \frac{Z_B{}^* Z_O}{r_B + r_O}$ leads to a stronger overlap between t_{2g} orbitals of the B ions and p_π orbitals of the O ions along the *x*, *y*, and *z* directions forming wider conduction bands. Hence, wider and continuous equipotential passages through –O–B–O–B–O– chains are formed and being expanded for the partially filled *d*-orbitals of the B ions, resulting in metal-like conduction in ABO_3. If the B ion is partially replaced by a different transition metal ion B* the conduction pathways change into –O–B–O–B*–O– chains and this leads to a modification of the flat potential, i.e., charge carrier trapping potential (Nakamura, private communication). For $A(B_{1-x}B^*_x)O_3$ compositions the metal-like conductivity can break at lower temperatures and semi-conductivity may appear when the B and B* ions are distributed at random (Nakamura, private communication). In the case of a deviation from oxygen stoichiometry, oxygen vacancies are introduced into the lattice at the expense of two electron holes and can act as scattering centers for holes. The flat equipotential is then further modified, i.e., $-O-B-O-B^*-\left[V_O^{\bullet\bullet}\right]-B-O-B^*-O-$. It is assumed that in a comparison with scattering mechanisms in traditional semi-conductors, like Si and GaAs, (1) lattice scattering involving collisions with thermally agitated lattice atoms/ions and (2) ionized impurity (i.e., donor-site and/or acceptor-site) scattering can occur. In the cubic perovskites, $\left(A'_{1-x}A'_x\right)\left(B'_{1-y}B'_y\right)\left[V_O^{\bullet\bullet}\right]_\delta O_{3-\delta}$, ionized impurity scattering will occur. Here, the oxygen vacancies play the role of impurity scattering centers, because they have an effective positive charge like the electron holes. Their concentration increases with increasing temperature, due to the increase in the deviation from stoichiometry. Therefore, a decreased electrical conductivity with increasing temperature, i.e., metal-like conductivity was found in BSCF materials at high temperatures.

The previous discussion is valid at higher temperatures (>450 °C) for all compositions, except for the one with $x=0.5$ and $y=0.8$, the Co richest one. In this material, we observed after the decreasing conductivity between 450 and 800 °C another increase with temperature up to 970 °C. This is again semi-conductivity behavior. According to Eq. 7, Co gets reduced from the valence state of 3+ towards 2+, as also found in a similar composition by Harvey et al. [33]. This is in accordance with the weight loss data for temperatures higher than 800 °C in Fig. 4 as well.

Summary and conclusions

The $Ba_xSr_{1-x}Co_yFe_{1-y}O_{3-\delta}$ compositions show thermally activated *p*-type semi-conductivity up to 450 °C with the highest value up to 1.46×10^4 S/m. The electrical conductivity of the BSCF materials exhibits a transition from semi-conductivity to metal-like conductivity from room temperature up to 970 °C in air. Strontium-rich compositions exhibit higher electrical conductivity with lower activation energy than barium-rich compositions. Iron-rich compositions have stronger metal-like conductivity behavior and lower activation energy than cobalt-rich compositions. The semi-conductivity is explained by a small-polaron hopping mechanism. The metal-like conductivity is attributed to the overlap of transition metal *d*-orbitals and oxygen *p*-orbitals at high temperatures, i.e., above 450 °C, and the role of oxygen vacancies as impurity scattering centers being most pronounced for the compositions rich in Fe and rich in Sr.

Acknowledgements The authors acknowledge financial support by the Swiss National Science Foundation grant Scopes 2009–2012: JRP Project IZ73Z0_128185/1 and Dr. Bieberle-Hütter, Dr. Martynczuk, and Dr. Rupp for helpful discussions.

References

1. Minh NQ (1993) J Am Ceram Soc 76(3):563
2. Kamata K, Nakajima T, Hayashi T, Nakamura T (1978) Mater Res Bull 13(1):49
3. Teraoka Y, Nobunaga T, Okamoto K, Miura N, Yamazoe N (1991) Solid State Ionics 48(3–4):207
4. Chen K, Lu Z, Chen X, Ai N, Huang X, Du X, Su W (2007) J Power Sources 172(2):742
5. Tai L-W, Nasrallah MM, Anderson HU, Sparlin DM, Sehlin SR (1995) Solid State Ionics 76(3–4):259
6. Tai L-W, Nasrallah MM, Anderson HU, Sparlin DM, Sehlin SR (1995) Solid State Ionics 76(3–4):273
7. Xia C, Rauch W, Chen F, Liu M (2002) Solid State Ionics 149(1–2):11
8. Kim CH, Qi G, Dahlberg K, Li W (2010) Science 327(5973):1624
9. Shao Z, Yang W, Cong Y, Dong H, Tong J, Xiong G (2000) J Membr Sci 172(1–2):177
10. Shao Z, Xiong G, Tong J, Dong H, Yang W (2001) Sep Purif Technol 25(1–3):419
11. Shao Z, Haile SM (2004) Nature 431:170
12. Jiang GS, Song CL, Li DC, Feng SJ, Wei L, Chen CS (2004) Chin J Chem Phys 17(1):75
13. Li S, Sun MT, Ji SJ, Sun JC (2005) Chin J Inorg Chem 21(8):1265
14. Wei B, Lu Z, Li S, Liu Y, Liu K, Su W (2005) Electrochem Solid-State Lett 8(8):A428
15. Ge L, Zhou W, Ran R, Liu S, Shao Z, Jin W, Xu N (2007) J Membr Sci 306(1–2):318
16. Ge L, Ran R, Zhang K, Liu S, Shao Z (2008) J Membr Sci 318(1–2):182
17. Zeng P, Chen Z, Zhou W, Gu H, Shao Z, Liu S (2007) J Membr Sci 291(1–2):148
18. Wei B, Lu Z, Huang X, Miao J, Sha X, Xin X, Su W (2006) J Eur Ceram Soc 26(13):2827
19. Chen Z, Ran R, Zhou W, Shao Z, Liu S (2007) Electrochim Acta 52(25):7343
20. Zhao H, Shen W, Zhu Z, Li X, Wang Z (2008) J Power Sources 182(2):503
21. Yang Z, Harvey AS, Infortuna A, Gauckler LJ (2009) J Appl Crystallogr 42(2):153
22. Shannon RD (1976) Acta Crystallogr A A32:751
23. Carter S, Selcuk A, Chater RJ, Kajda J, Kilner JA, Steele BCH (1992) Solid State Ionics 53–56(Part 1):597
24. Goodenough JB (1966) J Appl Phys 37(3):1415
25. Huang C-Y, Huang T-J (2002) J Mater Sci 37(21):4581
26. Koc R, Anderson HU (1995) J Eur Ceram Soc 15(9):867
27. Stevenson JW, Armstrong TR, Carneim RD, Pederson LR, Weber WJ (1996) J Electrochem Soc 143(9):2722
28. Goodenough JB (1967) Phys Rev 164(2):785
29. Emin D, Holstein T (1969) Ann Phys 53(3):439
30. Wang H, Tablet C, Yang W, Caro J (2005) Mater Lett 59(28):3750
31. McIntosh S, Vente JF, Haije WG, Blank DHA, Bouwmeester HJM (2006) Solid State Ionics 177(19–25):1737
32. McIntosh S, Vente JF, Haije WG, Blank DHA, Bouwmeester HJM (2006) Chem Mater 18(8):2187
33. Harvey AS, Litterst FJ, Yang Z, Rupp JLM, Infortuna A, Gauckler LJ (2009) Phys Chem Chem Phys 11(17):3090
34. Harvey AS, Yang Z, Infortuna A, Beckel D, Purton JA, Gauckler LJ (2009) J Phys Condens Matter 21(1):015801
35. Arnold M, Xu Q, Tichelaar FD, Feldhoff A (2009) Chem Mater 21(4):635
36. Trofimenko NE, Ullmann H (2000) J Eur Ceram Soc 20(9):1241
37. Mineshige A, Inaba M, Yao T, Ogumi Z, Kikuchi K, Kawase M (1996) J Solid State Chem 121(2):423
38. Tokura Y (2003) Phys Today 56(7):50
39. Kamata K, Nakamura T, Sata T (1974) Bull Tokyo Inst Technol 120(541.67:549.51):73